Circulation Response to Fast and Slow MJO Episodes

PRIYANKA YADAV

Climate Dynamics Program, and Department of Atmospheric, Oceanic, and Earth Sciences, George Mason University, Fairfax, Virginia

DAVID M. STRAUS

Department of Atmospheric, Oceanic, and Earth Sciences, George Mason University, Fairfax, Virginia

(Manuscript received 12 September 2016, in final form 16 January 2017)

ABSTRACT

Fast and slow Madden–Julian oscillation (MJO) episodes have been identified from 850- and 200-hPa zonal wind and outgoing longwave radiation (OLR) for 32 winters (16 October–17 March) 1980/81–2011/12. For 26 fast cases the OLR took no more than 10 days to propagate from phase 3 (convection over the Indian Ocean) to phase 6 (convection over the western Pacific). For 8 slow cases the propagation took at least 20 days. Fast episode composite anomalies of 500-hPa height (Z500) show a developing Rossby wave in the mid-Pacific with downstream propagation through MJO phases 2–4. Changes in the frequency of occurrence of the NAO+ weather regime are modest. This Rossby wave is forced by anomalous cooling over the Maritime Continent during phases 2 and 3 (seen in phase-independent wave activity flux). The upper-level anticyclonic response to phase-3 heating is a secondary source of wave activity. The Z500 slow episode composite response to MJO phases 1 and 2 is an enhanced Aleutian low followed by a North American continental high. Following phase 4 the development of an NAO+ like pattern is seen over the Atlantic, transitioning to a strong NAO− pattern by phase 8. A dramatic increase in frequency of the NAO+ weather regime follows phases 4 and 5, while a strong increase in NAO− regime follows phases 6 and 7. The responses to MJO-related heating and cooling over the Indian and western Pacific Oceans in phases 1–4 provide a source for wave activity propagating to North America, augmented by storm-track anomalies.

1. Introduction

The tropical intraseasonal variations included in what we know as the Madden–Julian oscillation (MJO) encompass not only a broad band of eastward-propagating circulation anomalies, but large deep anomalies in diabatic heating and upper-level divergence [see Zhang (2005) for a review]. The midlatitude responses to the MJO heating and divergence anomalies can be characterized in many ways (e.g., Cassou 2008, hereafter C08; Lin et al. 2009; Seo and Son 2012; Riddle et al. 2013; Henderson et al. 2016; Mundhenk et al. 2016, among many others). This body of work raises the prospect of enhanced extratropical predictability on intraseasonal time scales.

The approach almost universally taken to diagnose the extratropical manifestations of the MJO in observations, reanalyses, and models is based on the multivariate principal component analysis proposed by Wheeler and Hendon (2004), which utilizes upper- and lower-level zonal winds combined with outgoing longwave radiation (OLR). The synthesis of the leading two modes yields two time-dependent, normalized indices [termed Real-time Multivariate MJO index 1 (RMM1) and 2 (RMM2)] that describes an envelope of circulation fields and OLR (hence inferred large-scale convection) propagating eastward with a period of very roughly 20–70 days. The leading pair of modes can thus be represented in a two-dimensional phase space in terms of amplitude and phase, with the propagation seen as angular motion (Wheeler and Hendon 2004). Such diagrams are very widely used to represent the projection of individual episodes onto the leading two modes (e.g., see Lin et al. 2008; Kunio et al. 2013). Composites of extratropical fields based on phase (with the condition of normalized amplitude exceeding a threshold) have been used extensively to study the

Corresponding author e-mail: David M. Straus, dstraus@gmu.edu

DOI: 10.1175/MWR-D-16-0352.1

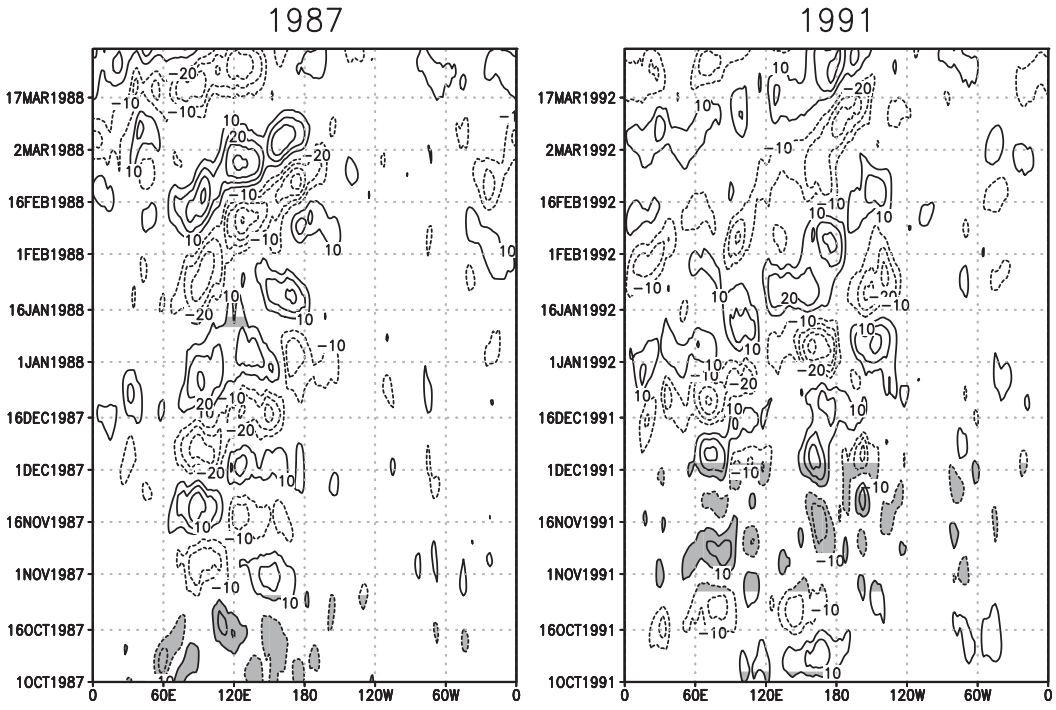

FIG. 1. Observed OLR averaged from 15°S to 15°N as a function of time for the extended winter (left) October 1987–March 1988 and (right) October 1991–March 1992. The contour interval is 10 W m^{-2}. The OLR has been filtered to retain periods of 20–100 days. Periods when the amplitude of the MJO index is less than 1.0 are shaded.

Northern Hemisphere upper-level streamfunction response (Matthews et al. 2004; C08; Moore et al. 2010; Henderson et al. 2016). The underlying assumption behind the use of composites is that the set of atmospheric states assigned to a particular MJO phase (with large enough amplitude) provide a common forcing for the extratropics. This is consistent with the modeling work of, for example, Matthews et al. (2004), who argue that observed extratropical circulation anomalies (obtained from time-lagged regression onto MJO composite heating) are explained as the directly forced response to the tropical heating 10–20 days earlier.

Even within the multivariate principal component framework one notes the variety in the individual observed episodes of the MJO, which show substantial changes in the phase speed and amplitude with time, as in Fig. 15 of Lin et al. (2008) and Fig. 7 of Kunio et al. (2013). Some episodes of MJO convection transit from the Indian Ocean to the western Pacific in less than 10 days, while others take longer than 20 days, and some never propagate into the Pacific at all (Kim et al. 2014). Figure 1 shows several examples of longitude–time plots based on observed daily OLR, averaged between 15°S and 15°N (see section 2 for details). During the extended winter season October 1987–March 1988, several episodes of organized convection (indicated by the centers of low OLR) propagate between the Indian Ocean and western Pacific in roughly 8 days, while during the winter of 1991/92, the figure shows (i) a slowly propagating episode, taking 22 days (10 February–3 March) to make the transit; (ii) a fast case, taking 9 days to transit (25 December–2 January); and (iii) an episode in which the convection never transits to phase 6 (starting 16 October). The methodology for determining the speed of propagation is discussed in section 2.

The distinction between fast and slow episodes of propagating MJO has not been considered previously, but is of potential importance for several reasons. The time lags between a state in a given phase of the MJO and both its previous and subsequent phase will be different for fast and slow MJOs; pooling them together (as has been done extensively in the past) makes it difficult to attribute time-lagged composite circulation states to specific locations of the heating and cooling. From another point of view, the MJO evolving heating and cooling at one particular time may be thought of as sources for wave trains, which in general interfere with each other (Lin et al. 2010; Straus et al. 2015). The remote response at any point some time later will involve the sum of these wave trains, each having traveled a different distance to reach the given point. The propagation speed of the heating and cooling will thus in

principle affect the remote response. Recent work by Branstator (2014) reinforces this point: in model calculations, short (2 day) pulses of equatorial heating generate wave trains whose eastward and poleward propagation is seen to develop far beyond the lifetime of the pulses themselves. From Fig. 3 of Branstator (2014), it becomes clear that the remote responses to a series of eastward-moving pulses would interfere with each other, either constructively or destructively, in a manner that depends on the motion of the pulses.

The overall goal of this paper is to separately diagnose the remote Northern Hemisphere responses to fast and slow episodes of MJO propagation during boreal winter in order to determine whether there are qualitative differences between these sets of responses and their relationships to the MJO-related tropical heating. For this purpose the traditional multivariate principal component analysis is quite adequate. To achieve our goal, we address the following specific questions:

- What significant differences are seen in the composite and lag composite response of the extratropical circulation height and streamfunction fields as function of MJO episode between fast and slow episodes?
- Are there significant differences in the evolution of wave-activity flux between fast and slow episodes?
- Do the established relationships between the MJO and Euro-Atlantic (EA) weather regimes (C08; Lin et al. 2009) depend on the speed of evolution of the MJO heating?
- Do differences in the associated storm tracks between fast and slow episodes play a role in the propagation of eddies?

In section 2 we discuss the data and analysis methods. Section 3 shows the composite anomalies of the 500-hPa geopotential height field (Z500) for fast episodes in all MJO phases. To relate these anomalies to the MJO heating, we also present the MJO-related OLR, streamfunction, and associated phase-independent wave activity composites. The corresponding composite anomalies for the slow episodes are shown in section 4. The response of the Euro-Atlantic weather regimes to the MJO is assessed separately in section 5 for fast episodes, slow episodes, and all episodes. The discussion is given in section 6 and the summary and conclusions are given in section 7.

2. Data and methods

a. Data and filtering

Once-daily upper-air data fields of 500-hPa height (Z500) and horizontal winds at 850, 300, 250, and 200 hPa were obtained from the ERA-Interim (Dee et al. 2011). The horizontal winds were used to construct fields of streamfunction. Daily fields of OLR were obtained from the interpolated dataset provided by the National Oceanic and Atmospheric Administration (Liebmann and Smith 1996). All upper-air fields were interpolated onto Gaussian grid with resolution 128 × 64 (latitude × longitude).

For the diagnosis of the MJO, daily anomalies of OLR and zonal wind at 200 and 850 hPa were calculated by removing the climatological daily annual cycle consisting of the first 4 annual harmonics [following Ventrice et al. (2013) and Wang et al. (2014)]. A 201-point Lanczos filter was then used to construct intraseasonal (20–100 day) daily anomalies for the period 16 October–17 March (153 days) for the 32 winters 1980/81–2011/12.

The seasonal cycle of Z500, 250-hPa streamfunction and wave activity (see below), and temperature and winds at 850 hPa were computed by fitting a parabola to each variable at each grid point for the period 1 October–31 March for each winter, and then averaging the parabolic fit over all winters (Straus 1983). Subtracting this average seasonal cycle gave the raw daily anomalies, which were used in the calculations of all composite maps, as well as for the weather regime analysis.

However, to assess the storm-track heat transport, it was necessary to further filter the daily anomalies of meridional wind and temperature at 850 hPa to retain only high-frequency components (periods less than 10 days). These filtered series were available for the period 16 October–17 March for each winter. The high-frequency component was used to determine the storm-track-related meridional transport of sensible heat.

Composites of the horizontal components of the phase-independent wave activity flux **W** at 250 hPa (WA) were calculated using the formulation of Takaya and Nakamura (2001), as adopted from their Eq. (38):

$$\mathbf{W} = \frac{p\cos(\phi)}{2\|U\|}(W_\lambda, W_\phi, W_p) + \mathbf{C}_U M, \tag{1}$$

with

$$W_\lambda = \frac{U}{a^2\cos^2(\phi)}\left[\left(\frac{\partial\psi'}{\partial\lambda}\right)^2 - \psi'\frac{\partial^2\psi'}{\partial\lambda^2}\right] + \frac{V}{a^2\cos(\phi)}\left(\frac{\partial\psi'}{\partial\lambda}\frac{\partial\psi'}{\partial\phi} - \psi'\frac{\partial^2\psi'}{\partial\lambda\partial\phi}\right), \tag{2}$$

$$W_\phi = \frac{U}{a^2\cos(\phi)}\left(\frac{\partial\psi'}{\partial\lambda}\frac{\partial\psi'}{\partial\phi} - \psi'\frac{\partial^2\psi'}{\partial\lambda\partial\phi}\right) + \frac{V}{a^2}\left[\left(\frac{\partial\psi'}{\partial\phi}\right)^2 - \psi'\frac{\partial^2\psi'}{\partial\phi^2}\right]. \tag{3}$$

Here λ is longitude, ϕ is latitude, ψ' is the streamfunction anomaly, a is Earth's radius, p is pressure (in units of

1000 hPa), U and V are the basic-state zonal and meridional winds, M is the pseudomomentum (see Takaya and Nakamura 2001), and the phase velocity vector $\mathbf{C}_U$ is given by

$$\mathbf{C}_U = C\frac{\mathbf{U}}{\|\mathbf{U}\|}, \tag{4}$$

where $\mathbf{U} = (U, V)$, and C is the zonal phase speed of the wave.

In applying this formula we did not consider the vertical component W_p, and further assumed that the phase velocity [second term of Eq. (1)] is relatively small for the MJO episodes. [This is consistent with previous applications of this wave activity, such as that of Henderson et al. (2016).] The basic-state wind vector (U, V) was obtained from the wind components averaged over all slow or fast episodes. The perturbation streamfunction was obtained from the anomalies of the daily streamfunction for various phases of the MJO, computed separately for slow and fast episodes.

b. Defining MJO amplitudes and phases

Following Wheeler and Hendon (2004) and Waliser et al. (2009) we computed multivariate EOFs of filtered fields of OLR, u200, and u850 averaged between 15°S and 15°N. Each field was normalized by the square root of the zonal mean of the temporal variance. The normalized time series of principal components PC1 and PC2 were calculated by projecting the data onto the observed EOFs to obtain the two PCs that are divided by their respective standard deviations. The variance explained by EOF1 and EOF2 is 22.6% and 21.6%, respectively. The positive (negative) phase of EOF1 shows suppressed (enhanced) convection over Indian Ocean and enhanced (suppressed) convection over the western Pacific. The positive (negative) phase of EOF2 shows suppressed (enhanced) convection over the Maritime Continent region. Their combination shows an eastward-propagating MJO in convection anomalies. The daily amplitude of MJO is defined as $\sqrt{\mathrm{PC1}^2 + \mathrm{PC2}^2}$ while the phase angle is given as arctan(PC1/PC2). All days in which the phase angle lies within a given octant are considered to be in one of eight phases. Maps of the composites of OLR and low-level winds for the eight phases over all times when the amplitude exceeds 1.0 are given in Fig. 2 for reference. They agree well with those shown by, for example, C08 and Henderson et al. (2016). In this paper, only days for which the amplitude is larger than 1.0 are included in the composite maps.

c. MJO episodes

MJO episodes are identified based on the location of convection using the filtered OLR anomalies and their corresponding MJO phase. The full intraseasonal tropical anomaly OLR fields and MJO phase could then be matched to determine the strength of the convection during each individual MJO episode. It was observed that some episodes of MJO take 10 days or less to propagate from phase 3 (Indian Ocean) to phase 6 (west Pacific), while other episodes take much longer (>20 days). Cases when the convection did not propagate into the Pacific were also identified. To get an unambiguous determination of propagation time from phases 3 to 6, we considered only episodes in which the amplitude exceeded 1.0 for 3 consecutive days in phase 3, and subsequently for 3 consecutive days in phase 6. We do not require that the amplitude exceed 1.0 during phases 4 and 5, since during those phases the MJO crosses the Maritime Continent region and at these times may not be well represented by the two EOFs we have used (Wu and Hsu 2009). A histogram of the number of such episodes as a function of the length of time to propagate from phases 3 to 6 is given in Fig. 3. From this we define fast episodes as those reaching phase 6 within 10 days, and slow episodes as those that take 20 days or longer to reach phase 6. Episodes for which the amplitude exceeded 1.0 for three consective days only in phase 3 are considered nonpropagating episodes, termed IOnP. Three types of categories are thus defined as follows:

- Slow episodes in which the OLR minimum takes 20 or more days to propagate into the west Pacific (eight episodes);
- Fast episodes in which the OLR minimum takes 10 days or less to propagate into the west Pacific (26 episodes);
- IOnP episodes in which the OLR minimum is present in the Indian Ocean (phase 3) but does not propagate into west Pacific (phase 6) (17 cases).

For five of the slow episodes, continuous eastward phase propagation between phases 3 and 6 is evident (even with amplitude less than 1.0 in phases 4 and 5). The remaining three slow episodes seem to become stationary for a period during phase 5, over the Maritime Continent. Whether each of these episodes is part of a single MJO cycle or two unrelated (and incomplete) cycles is ambiguous.

The full dates of the slow and fast episodes identified, as well as of the nonpropagating (IOnP) episodes, are given in Table 1. For each episode, the center date for which the oscillation was in phase 3 with an amplitude

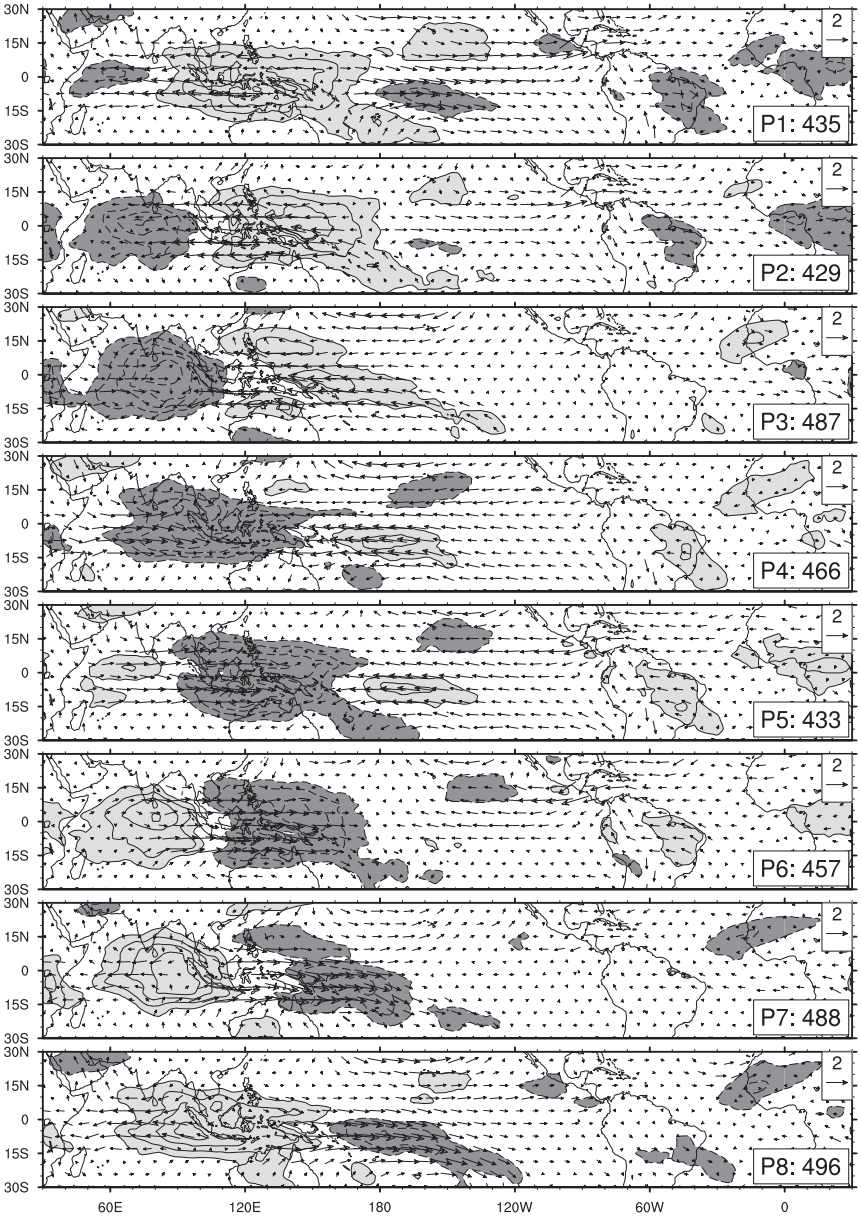

FIG. 2. Composites over the eight phases of the MJO. Anomalies of OLR shown with contour interval of 5 W m^{-2}, with no zero contour. Dark shading corresponds to values less than −5 W m^{-2}, and light shading to values greater than +5 W m^{-2}. Zonal winds at 850 hPa shown by arrows, units of m s^{-1}. Composites taken over all days in which the normalized amplitude of the MJO exceeds 1.0. See text for details.

exceeding 1 was first determined. The date corresponding to the previous phase 1 gave the start date, while the date corresponding to the subsequent phase 8 gave the end date. Note that three of the slow episodes occurred during moderate El Niño events: one during a strong event, one during a weak La Niña event, and three during non-ENSO winters. The initiation dates of both slow and fast are distributed throughout the winter, from October to March. There are episodes that take between 10 and 20 days to propagate between phases 3 and 6, which we have not used for further analysis (see Table 1), since we wanted to compare responses to the fastest episodes with those of the slowest. To see the equatorial OLR evolution, lag composites of OLR (averaged between 15°S and 15°N) for days 10–30 are calculated for phase 3 and shown in Fig. 4 for all

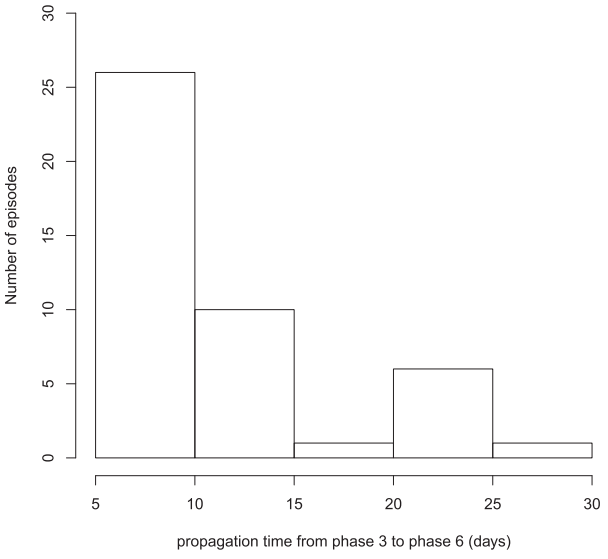

FIG. 3. Histogram of propagation time from phases 3 to 6.

episodes, the fast episodes, the slow episodes, and the IOnP episodes. Note that day 0 in the figure indicates the center of OLR is in the Indian Ocean (90°E), while the central longitude for phase 6 is 160°E.

d. Weather regimes

Weather regimes were computed from the daily Z500 series over the EA region: 20°–90°N, 90°W–30°E. The regimes were identified using a cluster analysis based on the *k*-means partitioning algorithm, as described in Michelangeli et al. (1995), Straus et al. (2007), and Straus (2010). We briefly review the method here. For the EA region, principal component analysis was carried out on the daily Z500 anomaly fields, with the leading six modes explaining nearly 70% of the total space–time variance. The cluster algorithm was carried out on the corresponding principal components (PCs). For a given number of clusters *k*, the algorithm assigns each state to a cluster by maximizing the ratio of the variance between cluster centroids (defined by the PC coordinates averaged over all states in that cluster) to the average intracluster variance (spread).

The significance of the partitioning for *k* ranging from 2 to 6 was determined by comparing the variance ratio obtained from the observed PCs to those obtained from analysis of a large number (100) of synthetic PC datasets, where in each synthetic dataset each PC is generated from a stochastic model that reproduces as much of the lagged autocorrelation structure of the corresponding

TABLE 1. Table of start and end dates for each type of episodes.

Slow episodes		Fast episodes		IOnP episodes		Intermediate episodes	
Start date	End date	Start date	End date	Start date	End date	Start date	End date
1 Nov 1984	21 Jan 1985	26 Oct 1985	23 Dec 1985	19 Oct 1981	17 Nov 1981	14 Dec 1982	24 Jan 1983
23 Dec 1986	4 Mar 1987	24 Dec 1985	6 Feb 1986	25 Dec 1981	1 Feb 1982	22 Jan 1985	14 Mar 1985
20 Jan 1992	16 Mar 1992	21 Oct 1986	24 Nov 1986	21 Nov 1982	13 Dec 1982	11 Jan 1988	26 Feb 1988
22 Nov 1993	7 Jan 1994	25 Oct 1987	27 Nov 1987	25 Jan 1983	9 Mar 1983	15 Dec 1989	6 Feb 1990
30 Jan 1998	17 Mar 1998	28 Nov 1987	10 Jan 1988	10 Dec 1983	7 Jan 1984	7 Feb 1990	17 Mar 1990
24 Oct 2001	7 Jan 2002	30 Dec 1988	14 Feb 1989	8 Jan 1984	27 Feb 1984	6 Jan 1997	17 Mar 1997
8 Jan 2002	8 Mar 2002	16 Oct 1990	30 Nov 1990	1 Dec 1990	6 Jan 1991	5 Jan 1999	22 Feb 1999
20 Dec 2009	6 Feb 2010	12 Dec 1991	19 Jan 1992	7 Jan 1991	8 Feb 1991	14 Jan 2004	27 Feb 2004
		6 Jan 1993	23 Feb 1993	16 Oct 1991	18 Nov 1991	2 Dec 2007	21 Jan 2008
		8 Jan 1994	4 Mar 1994	24 Feb 1993	16 Mar 1993	12 Feb 2012	16 Mar 2012
		27 Dec 1994	1 Feb 1995	29 Oct 1993	21 Nov 1993		
		16 Nov 1996	5 Jan 1997	1 Dec 1998	25 Dec 1998		
		7 Nov 2000	22 Dec 2000	19 Nov 1999	27 Dec 1999		
		23 Dec 2000	3 Mar 2001	20 Oct 2004	18 Nov 2004		
		24 Oct 2002	9 Dec 2002	10 Feb 2006	14 Mar 2006		
		10 Dec 2002	26 Jan 2003	16 Oct 2008	7 Nov 2008		
		27 Nov 2003	13 Jan 2004	25 Jan 2011	4 Mar 2011		
		16 Dec 2004	20 Jan 2005				
		1 Jan 2006	9 Feb 2006				
		12 Dec 2006	8 Feb 2007				
		9 Feb 2007	13 Mar 2007				
		22 Jan 2008	29 Feb 2008				
		18 Jan 2009	16 Feb 2009				
		26 Oct 2009	19 Dec 2009				
		16 Oct 2011	18 Nov 2011				
		19 Nov 2011	14 Dec 2011				

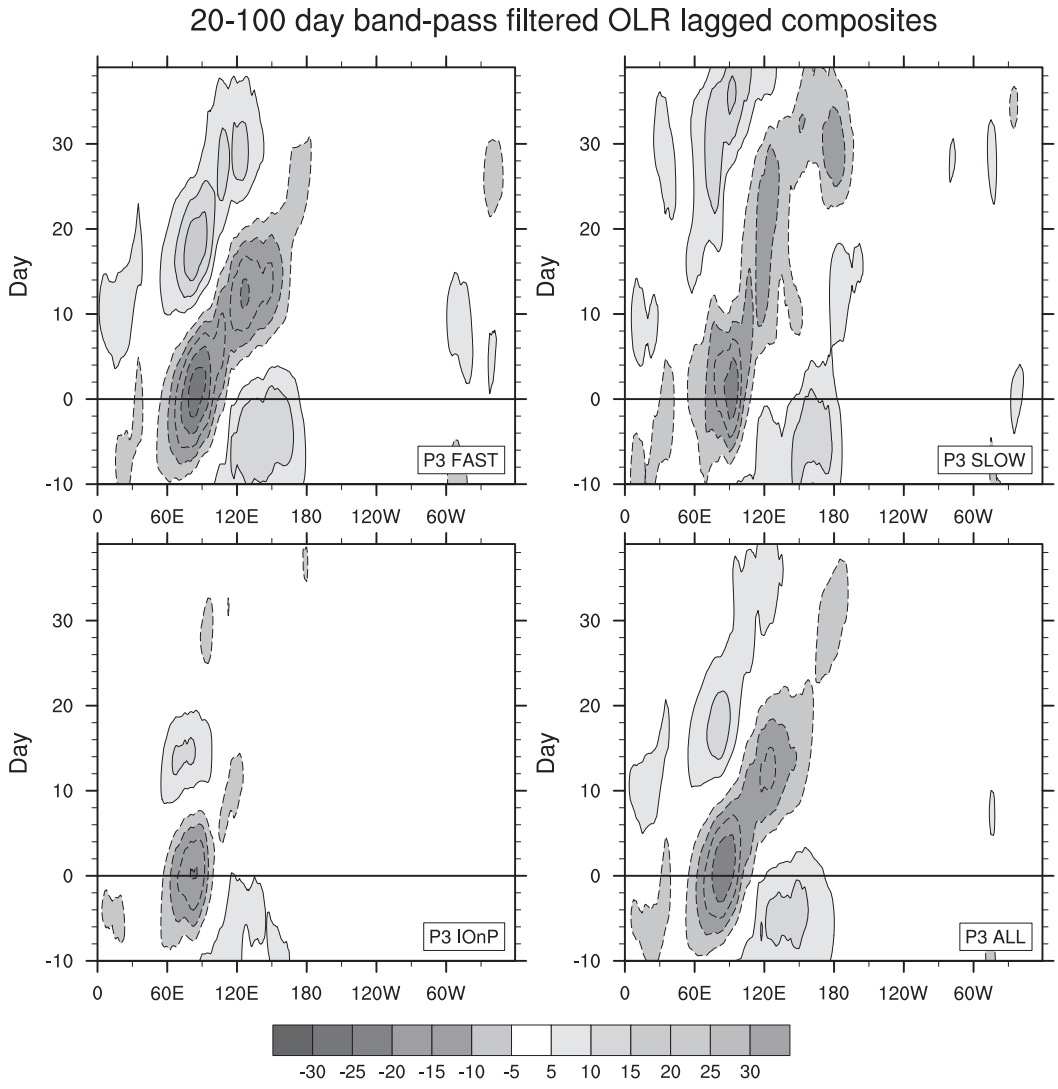

FIG. 4. Observed OLR (W m^{-2}) lag composites for episodes that remain in phase 3 (convection centered at 90°E) for at least three consecutive days with amplitude greater than 1.0. OLR is averaged over 15°S–15°N. Day 0 indicates the episode is in phase 3. (top left) Fast episodes, (top right) slow episodes, (bottom left) episodes that do not propagate into the Indian Ocean, and (bottom right) all episodes. See text for further details.

observed PC as possible. The percentage of synthetic datasets for which the variance ratio is *less than* the observed variance ratio gives a confidence level. The stochastic process used was based on the random phase approximation (Christiansen 2007) as modified by Straus (2010). The autocorrelation of individual observed PCs for all available lags (given the length of the season) is approximately preserved by this procedure (not shown). The confidence level tends to increase with k, so a simple approach is to take the minimum value of k for which this level exceeds a threshold, here taken to be 0.95.

For the EA region, $k = 4$ achieves this level, and the patterns obtained are the robust set encompassing the NAO+, NAO−, Atlantic ridge, and Scandinavian blocking patterns. These patterns, shown in C08, are quite robust to the period (definition of winter, years) and pressure level used (Vautard 1990). The NAO+ and NAO− refer to patterns that resemble the North Atlantic Oscillation, but are not precise opposites in the cluster analysis. The Scandinavian blocking pattern has a large ridge over western Europe while the Atlantic ridge shows high pressure over the central North Atlantic. Note that these last two patterns are not meant to summarize the regions where individual blocking events occur.

To study the lagged relationships between the eight phases of the MJO and the four North Atlantic circulation regimes, we compute the anomalous occurrence

of a given regime as a function of MJO phase and lag, with regimes lagging the MJO phases. We first calculate the anomalous percentage of regime occurrence in the same way as C08, taking into account *all* MJO episodes. Define $M_{k,\phi,n}$ as the number of occurrences in days of a regime (k) for a given MJO phase ϕ and lag n, and N_ϕ as the total number of days in that phase. Then the percentage of occurrence $P_{k,\phi,n}$ is given by

$$P_{k,\phi,n} = 100 \times M_{k,\phi,n}/N_\phi. \quad (5)$$

Given the climatological percentage of occurrence C_k of regime k, we compute the anomalous percentage $A_{k,\phi,n}$ for regime k associated with the particular phase and lag:

$$A_{k,\phi,n} = 100 \times (P_{k,\phi,n} - C_k)/C_k. \quad (6)$$

The quantity $A_{k,\phi,n}$ was also computed separately for each type of episode: fast, slow and IOnP.

e. *Statistical significance of composites and weather regime frequency of occurrence*

To test the null hypothesis that the frequency of occurrence of the weather regimes *within a given MJO phase* is independent of the type of episode, a chi-squared test was run on the contingency table (for each MJO phase) containing the number of occurrences within each type of episode (three rows: IOnP, slow and fast) and in each regime (four columns). A separate chi-squared test for all cases (total category) was run on the contingency table containing the number of occurrences within each weather regime (four columns) and eight MJO phases (eight rows). The latter tests the null hypothesis that the occurrence of weather regimes is independent of MJO phase, and is similar to the test used by C08. The 90% confidence level was used to indicate significance.

To test the significance of Z500, WA and P250 composite anomalies, a large number (1000) of synthetic datasets were generated by scrambling the original data: each sequence of maps within a given MJO phase is replaced by a sequence of the same length starting from a randomly chosen map within the original dataset (bootstrap with replacement). This method of generating the synthetic datasets preserves the number of degrees of freedom. Composites based on the correct dates of the various episodes (but using the maps of the scrambled synthetic datasets) were computed. The percentage of times for which the absolute value of the observed anomaly composite (at a given grid point) exceeded those in the synthetic datasets gives the confidence level. All the figures in this paper show anomaly composites for which this level exceeds 90%.

3. Extratropical response to the fast MJO episodes

Composites of daily anomalies of Z500 and streamfunction with wave activity vectors at 250 hPa for each phase of the MJO are presented in this section and the following one. A reasonable hypothesis is that the anomalous circulation associated with a given phase of the MJO is a response to tropical MJO-related diabatic heating at an earlier time. To the extent that MJO episodes maintain a large amplitude from the end of one cycle (phases 7 and 8) to the beginning of the next (phases 1 and 2), the response in phases 1 and 2 can be interpreted as being due to the diabatic heating in the later phases of the previous cycle. Many (but not all) MJO episodes that are strong in phases 7 and 8 maintain that strength to the next cycle.

a. *500-hPa height in Northern Hemisphere*

Composites of the daily Z500 anomaly for fast episodes are shown as a function of MJO phase in Fig. 5. Shaded regions are significant at the 90% confidence level. The phase 1 map shows a high extending northeast from the Gulf of Alaska into the Beaufort Sea and beyond to Baffin Bay. This feature has disappeared by phase 2. The maps for phases 3–5 are dominated by a wave train consisting of a large high pressure system over the central Pacific, low over the Gulf of Alaska, and a high over northeastern North America. Clear evidence of downstream development is seen. Each of these features move slowly from phase to phase, but the amplitude of features downstream (e.g., to the east) grows from phases 3 to 5, while the upstream features decay. This wave train is continued into the North Atlantic in phases 4 and 5. The response for phase 5 is similar to that of the positive phase of the NAO (NAO+), although the low over the Atlantic is shifted southward. By phase 6 the amplitudes decrease, but the high pressure system over the Pacific, which has migrated to the northeast, grows again in phase 7. The lag composites for days 5, 10, and 15 (Z500 lagging the MJO phase, not shown) show remarkable consistency: the day-5 composite from phase n looks very much like the simultaneous composite from phase $n + 1$, the day-10 composite from phase n looks very much like the simultaneous composite from phase $n + 2$, and so forth.

b. *Global 250-hPa streamfunction and wave activity response*

The composites of streamfunction P250 and wave activity vectors at 250 hPa, along with tropical OLR, shown in Fig. 6 for the domain north of 10°S, put these responses in a wider context. The P250 response in the subtropical North Pacific west of the date line in phases 2

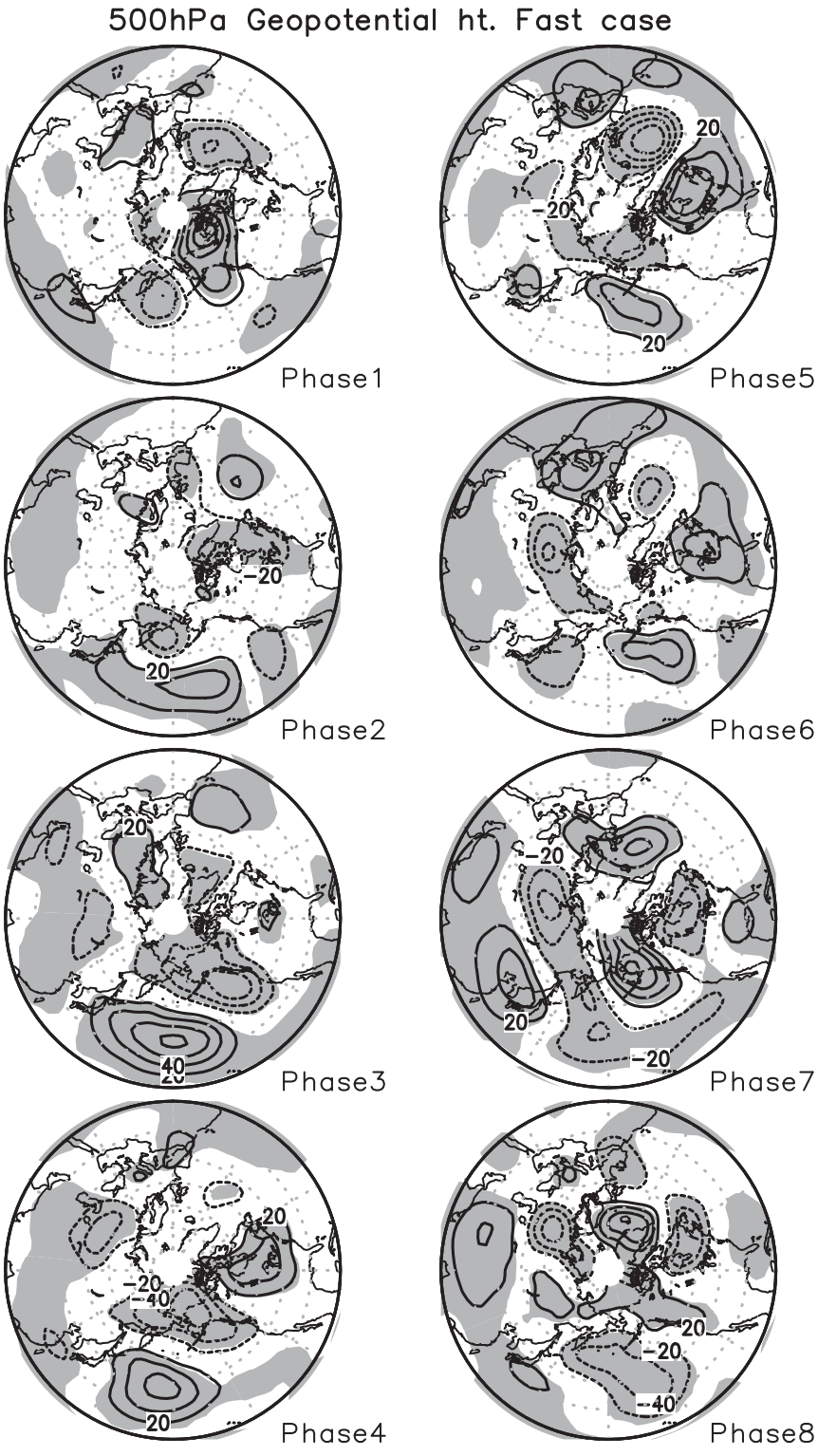

FIG. 5. Composite anomalies of daily 500-hPa height for fast MJO episodes for periods when the MJO is in each of eight phases with normalized amplitude exceeding 1.0. (left) Phases 1–4 and (right) phases 5–8. Units are m. Shaded regions show areas with statistical confidence at or above 90% based on bootstrap resampling. The domain is north of 20°N. See text for details.

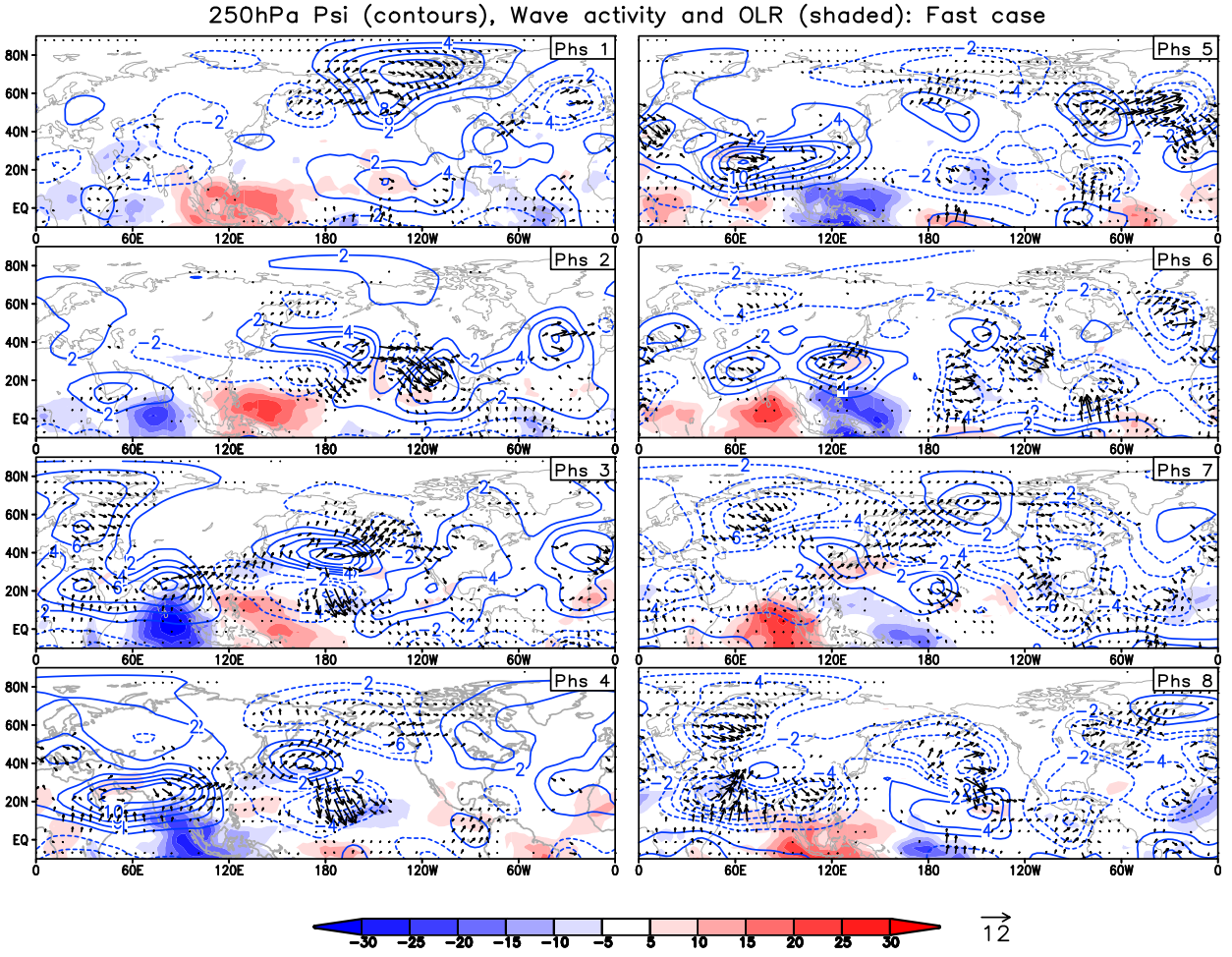

FIG. 6. Composites of daily 250-hPa streamfunction (contours), horizontal components of phase-independent wave activity (arrows), and tropical OLR for fast episodes, when the MJO is in each of eight phases with normalized amplitude exceeding 1.0. (left) Phases 1–4 and (right) phases 5–8. The domain is north of 10°S. See text for further details. The contour interval is 1.0×10^{-6} m^2 s^{-1} for streamfunction. Only arrows with statistical confidence at or above 90% based on bootstrap resampling are shown. Units of wave activity are m^2 s^{-2}, with the arrow scale indicated.

and 3 appears to be a local wave train developing in response to the Pacific cooling (positive OLR anomalies). The positive anomalies act as a wave source for propagation downstream over North America in phases 2–4, as seen in the wave activity vectors. The subtropical high situated to the west of the MJO-related heating over the Indian Ocean intensifies from phases 3 to 5, and provides an additional source of wave activity starting in phase 3. By phase 4 this high augments the subtropical source of wave activity toward North America. Note that by phase 5 the wave activity shows propagation over North America, across the Atlantic, and toward the equator near 0° longitude. The continuity of the wave propagation from the Indo-Pacific tropical regions toward the North Pacific is apparent again in phase 7, when the upper-level streamfunction response resembles that of the Arctic Oscillation.

4. Extratropical response to the slow MJO episodes

a. 500-hPa height in Northern Hemisphere

Composites of the daily Z500 anomaly for slow episodes are shown as a function of MJO phase in Fig. 7. The response during phases 1 and 2 are surprisingly similar to the response during an El Niño event, with a subtropical eastern Pacific high, enhanced Aleutian low, and in phase-2 positive anomalies over north-central and northeastern North America and negative anomalies over the Gulf of Mexico and southeastern North America. Four of the eight slow episodes in fact took place during El Niño events: one during a (weak) La

Niña event, and three during ENSO-neutral years, as shown in Table 1. A strong low over the northeast Pacific develops in phase 4, which by phase 5 has propagated across northern North America to southern Greenland, setting up the negative center of the NAO+ pattern over Greenland. This low moves equatorward in phase 6 and the eastward in phase 7, leading to the development of a very strong NAO− pattern in phase 8.

The development of the NAO+ like response following phase 4 is further shown in Fig. 8, which shows the lagged composites for phase 4 (at lags +5, +10, and +15 days). Note that in contrast to the fast episodes, the lagged composites from the slow episodes do not reproduce the composites at later MJO phases in a regular way. This is a consequence both of the longer transit times of the slow episodes and the limited sample.

b. *Global 250-hPa streamfunction and wave activity response*

Figure 9 gives the composites of 250-hPa streamfunction P250, OLR, and wave activity vectors for all phases of the MJO. The composites for phases 1 and 2 show the expected development of heating (negative OLR anomalies) in the Indian Ocean with positive anomalies (indicating subsidence) over the western Pacific, but also heating over the eastern Pacific (especially in phase 1), possibly a residual from the contributing El Niño years. The subtropical P250 response in phases 1 and 2 shows the expected negative (cyclonic) anomalies to the west of the central Pacific cooling and the positive anomalies to the west of the eastern Pacific heating. As the Indian Ocean heating propagates eastward into the western Pacific in phases 3–5, the positive response to its west dominates. The wave activity vectors indicate eastward and equatorward propagation from the Indian Ocean toward the central Pacific during phases 1 and 2; in the central Pacific a tropical source is hinted at in phase 2. The source for the strong wave activity flux across North America and into the Atlantic is located in the subtropics in phase 3 but moves northward during phases 4 and 5. In phase 3, the wave activity vectors seem to emanate from subtropical centers, which themselves can be interpreted as the direct response to the tropical MJO heating.

The upper-level phase-independent horizontal wave activity vectors show Pacific subtropical and midlatitude sources for both fast and slow episodes as they develop, although these sources differ in details and timing. For the fast episodes during phases 2–4, the wave train developing just eastward and poleward of the equatorial cooling (positive OLR) anomaly leads to a subtropical source of poleward- and eastward-directed wave activity. Poleward wave activity is also linked to the cooling anomalies in phase 7. During the slow cases, tropical and midlatitude sources of poleward wave activity are seen in the central and eastern Pacific during phases 1 and 2, possibly linked to early MJO activity from a previous episode. The midlatitude sources of eastward-propagating wave activity stay strong from phases 4 to 6, and again in phase 8.

One interesting difference is the relationship with the anomalies in the storm tracks, as measured by the slow episode composites of total and anomalous high-pass meridional heat transport at 850 hPa, shown in phases 3 and 4 for various lags in Figs. 10 and 11. For phase 4, the slow episode wave activity source region in the eastern Pacific is slightly downstream and poleward of the enhanced storm-track activity. This relationship is not seen for the fast episodes (for which the meridional heat transport is not shown). For enhanced storm-track activity to act a source of wave activity requires enough time for the synoptic eddies to respond in an organized manner to the tropical heating anomalies. This is more likely to occur during the more quasi-stationary slow episodes.

5. Weather regime response to the MJO

An alternative method for gauging the circulation response to the MJO is to determine the evolution of the population of the Euro-Atlantic weather regimes during and following the various MJO phases, as was done in C08. This measure of dominant response patterns will not always correspond on a one-to-one basis with those indicated by the composites shown in sections 3 and 4. A composite map may be dominated by a few instances of very strong anomalies, while the majority of states making up such a composite, although having smaller magnitude anomalies, may be assigned to a different weather regime. Figures 12 and 13 show the lagged relationships between the eight phases of the MJO and the four North Atlantic circulation regimes. This is similar to Fig. 3 of C08 in that it shows the anomalous percentage occurrence of a given regime as function of lag, with regimes lagging the MJO phases.

However, instead of showing the changes for all MJO occurrences, we show the changes for the fast and slow episodes defined in section 2, as well as for all episodes (total) for which the amplitude of the MJO exceeded 1.0. Fast, slow, and total results are shown in red, green and black bars, respectively. Results that did not pass the chi-squared significance test at the 90% level are not shown.

An increase in percentage anomaly as time lag increases (positive slope) is suggestive of a growing extratropical response to a particular phase of the MJO.

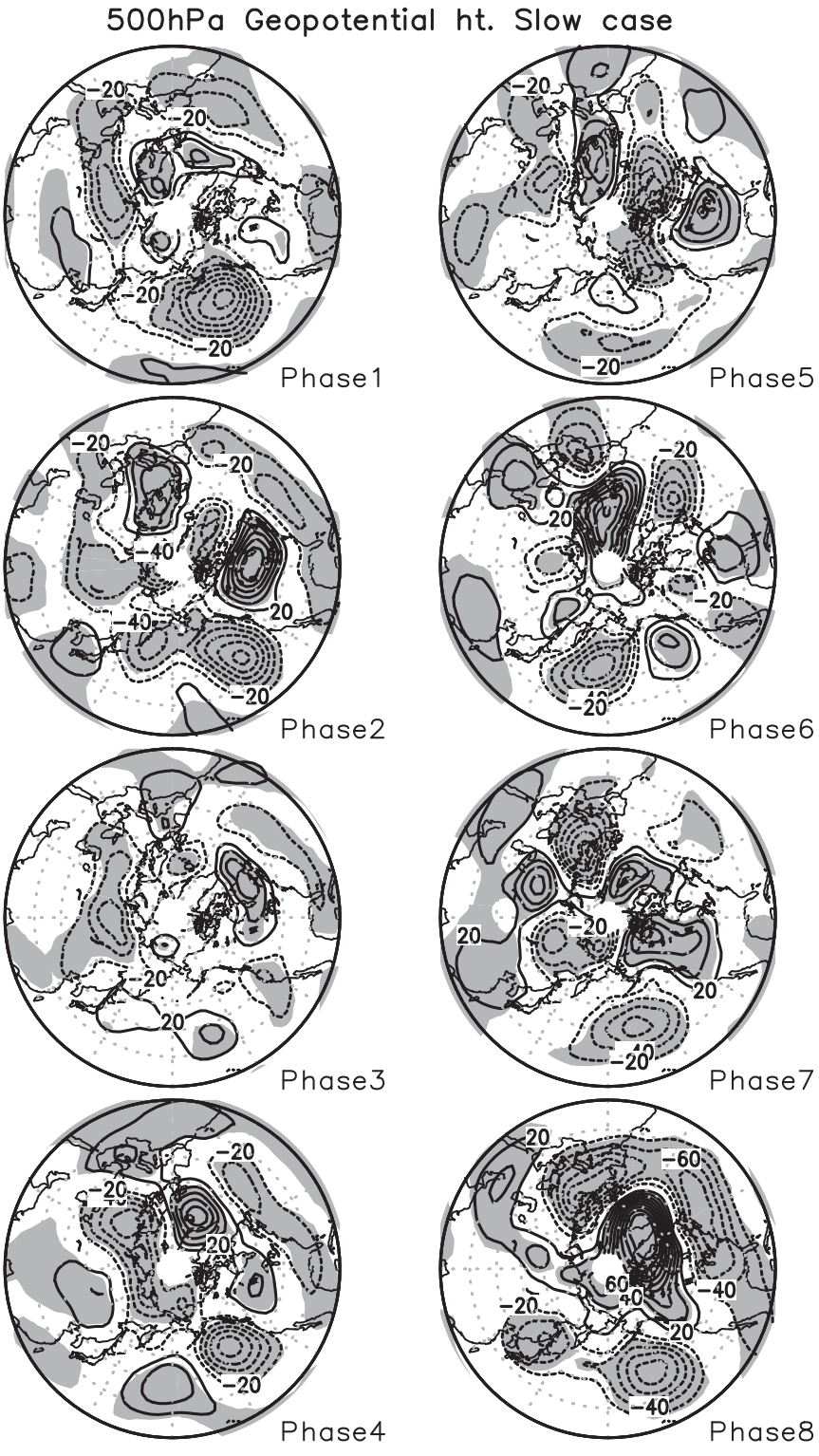

FIG. 7. Composite anomalies of daily 500-hPa height for slow MJO episodes for periods when the MJO is in each of eight phases with normalized amplitude exceeding 1.0. (left) Phases 1–4 and (right) phases 5–8. Units are m. Shaded regions show areas with statistical confidence at or above 90% based on bootstrap resampling. The domain is north of 20°N. See text for details.

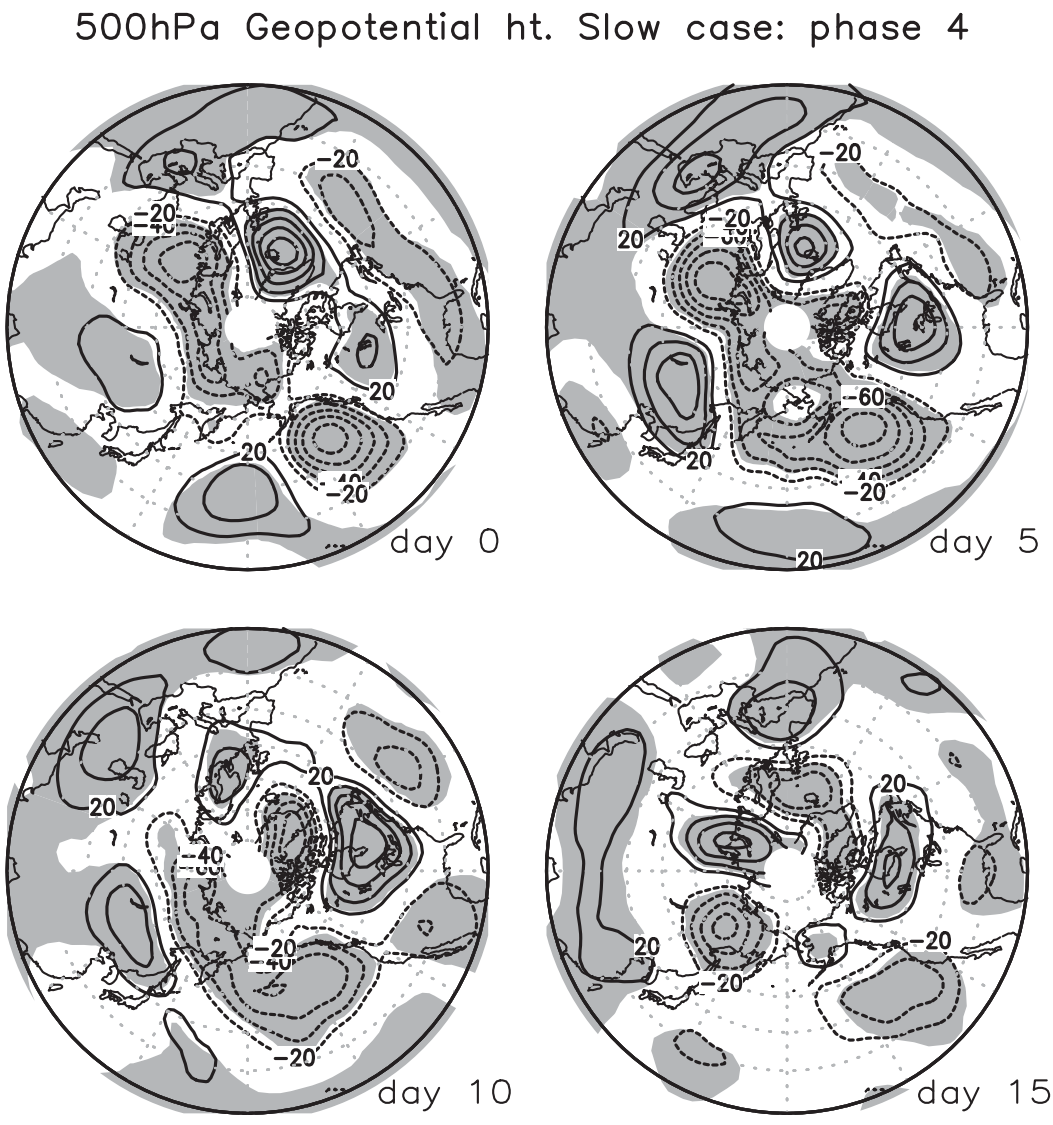

FIG. 8. Lag composite anomalies of daily 500-hPa height for slow MJO episodes (with normalized amplitude exceeding 1.0) for periods when the MJO is in phase 4 at (top left) lag 0, (top right) lag +5 days, (bottom left) lag +10 days, and (bottom right) lag +15 days. Units are m. Shaded regions show areas with statistical confidence at or above 90% based on bootstrap resampling. See text for details.

Increases in occurrence of the NAO+ regime for slow episodes can be seen after 13 days lag in phase 4, a response that amplifies to over 80% by day 15. An increase in NAO+ occurrence can also be seen from day 0 to day 15 in phase 5. For fast episodes, a modest increase can be seen starting from the start of phase 4. Considering all episodes (total), a very modest response is seen earlier, after about 10 days lag in phase 3.

The frequency of occurrence of the NAO− for slow episodes increases rapidly after 4 days from the start of phase 6 and exceeds 160% by phases 7–8. (We should note that while the highest percentage increase shown in the anomalous occurrence plots is 160%, the actual anomaly for phases 6–8 for NAO− during slow episodes exceeds this, reaching nearly 200%.) The fast cases and total category frequencies also increase rapidly here, reaching about 80%. Scandinavian blocking frequency anomalies increase almost from the start of phase 5, an increase in which both fast and slow episodes participate.

Some of the overall features seen in the results of C08 are noted here, but with some important differences. The modest NAO+ response in the total category for phase 3 after about 10 days is similar to C08, but the strong responses seen in the slow episodes after phases 4–5 are new. The slow episode changes for NAO− in

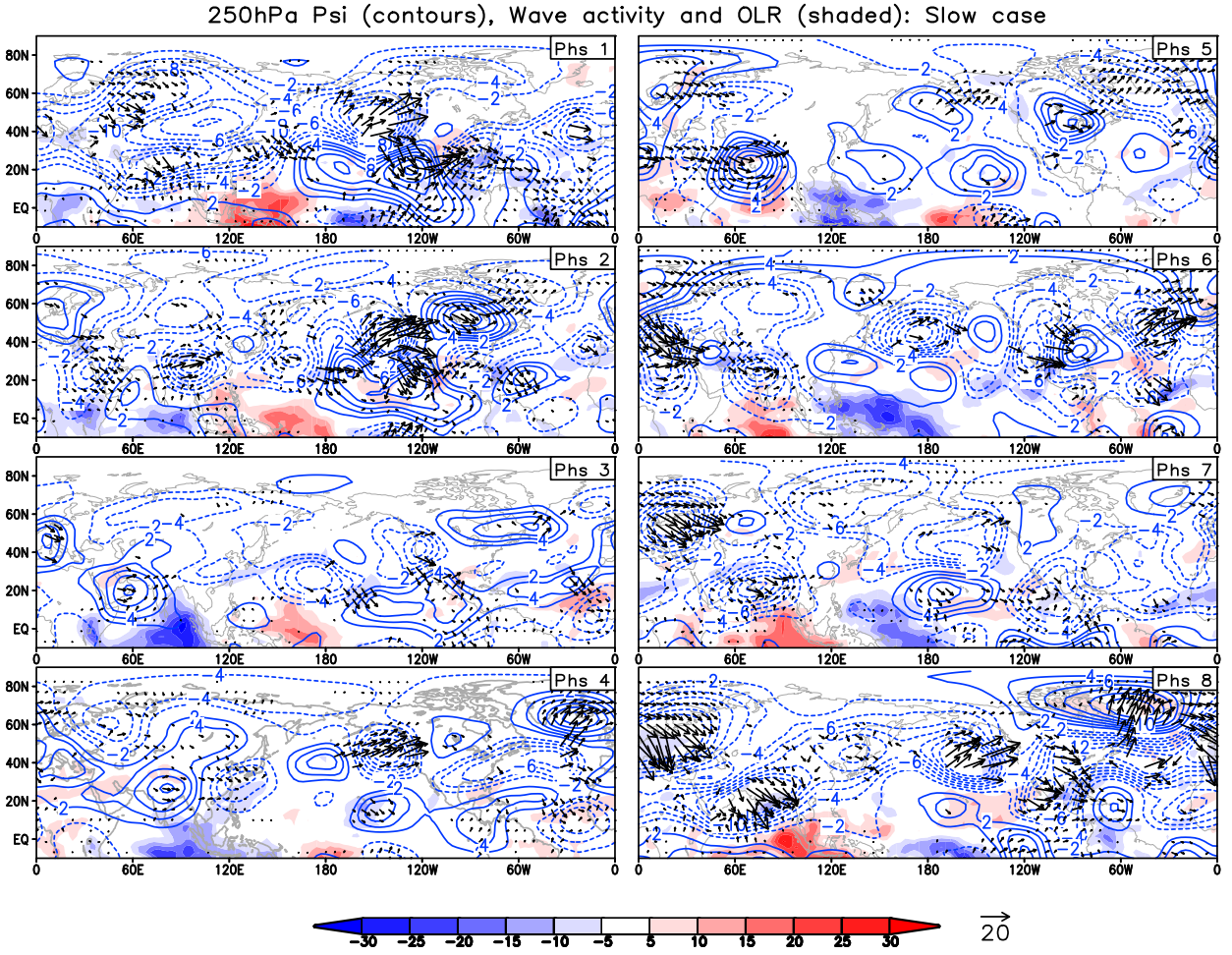

FIG. 9. Composites of daily 250-hPa streamfunction (contours), horizontal components of phase-independent wave activity (arrows), and tropical OLR for slow episodes for periods when the MJO is in each of eight phases with normalized amplitude exceeding 1.0. (left) Phases 1–4 and (right) phases 5–8. The domain is north of 10°S. See text for further details. The contour interval is 1.0×10^{-6} m^2 s^{-1} for streamfunction. Only arrows with statistical confidence at or above 90% based on bootstrap resampling are shown. Units of wave activity are m^2 s^{-2}, with the arrow scale indicated.

phase 6 are much larger here than in C08, indicating that the C08 changes in NAO− arise predominantly from slow MJO cases. Also, the increase in Scandinavian blocking occurrence for fast and slow episodes occurs in phase 5 in these results, somewhat earlier than in C08.

6. Discussion

a. *Comparison of fast and slow response episodes to previous work*

Since previous work has generally assessed the response to the MJO on the basis of phase only, including all strong MJO episodes, composites published by Vitart and Molteni (2010) and Henderson et al. (2016) combine both fast and slow episode responses, as well as those to the MJO episodes that do not propagate out of the Indian Ocean. Figure 7 of Vitart and Molteni (2010) show Northern Hemispheric maps of the combined (lag 0) Z500 response to phases 4 and 5 in their Fig. 7b, and to phases 1 and 8 in their Fig. 7d. The total phase 4 and 5 response includes elements of our Z500 response to fast episodes in phase 4 in the Pacific–North American region. Over the Euro-Atlantic region, our slow and fast Z500 responses in phase 5 are generally similar, and agree with the combined phase 4 and 5 total response of Vitart and Molteni (2010). Their combined response to phases 1 and 8 seems to be dominated by our slow response to phase 8, although some elements of our fast phase 8 response over the eastern Pacific and northeast North America can be seen. Vitart and Molteni (2010) also show responses lagged by 10 days from phase 3 (their Fig. 8b) and from phase 6 (their Fig. 8d). While the former shows elements

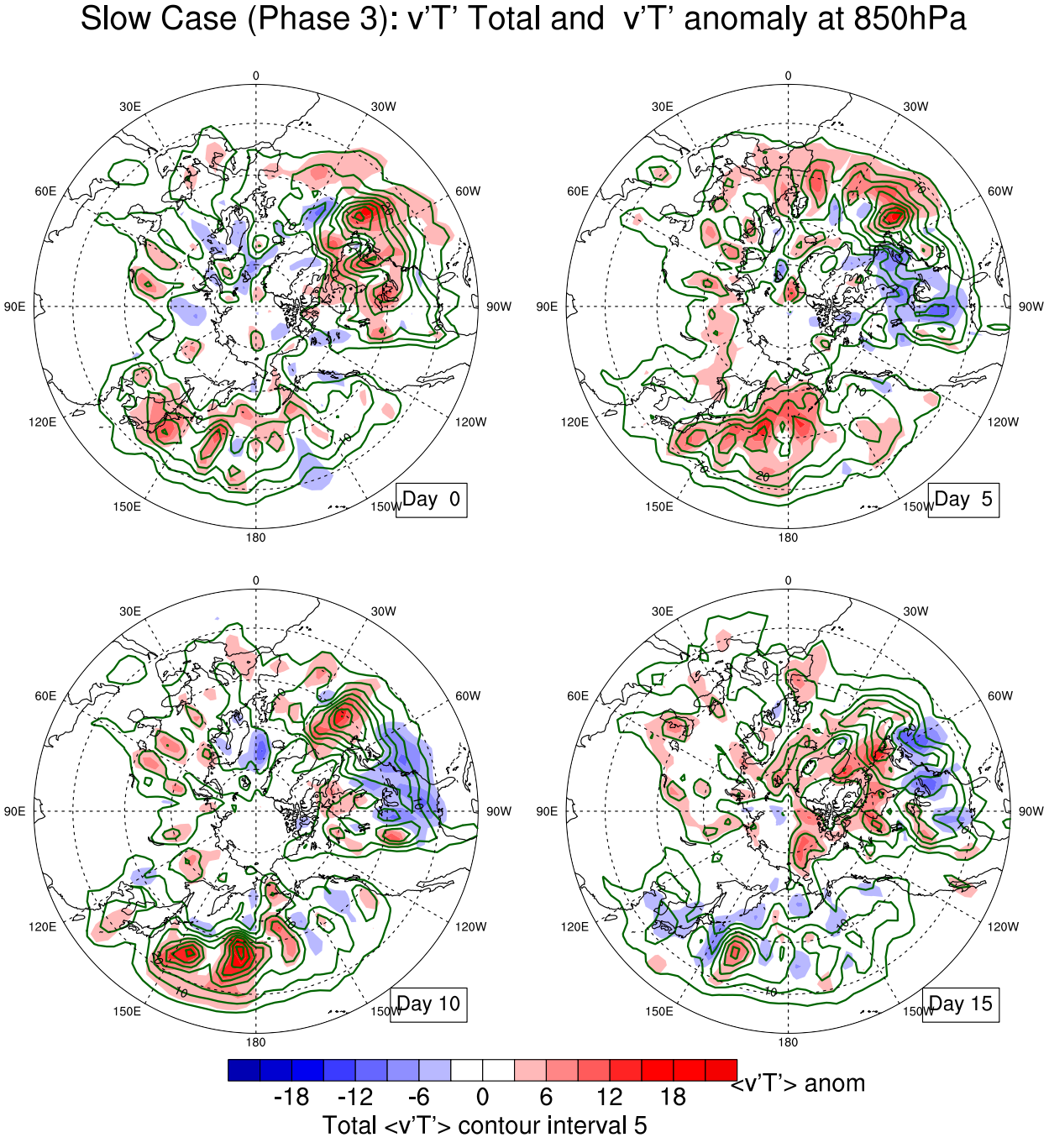

FIG. 10. Slow episode composites of covariance between high-pass meridional wind and temperature at 850 hPa (periods less than 10 days retained) for MJO phase 3 at lags 0, +5, +10, and +15 days (covariance lag MJO). Contours show total (interval of 5 m s^{-1} K), shading shows anomalies. See text for details.

of both our fast and slow responses at lag 10 (not shown), it more strongly agrees with the slow response. The lagged response to phase 6 is dominated by our corresponding lag 10 slow response (not shown).

Henderson et al. (2016) also show the Z500 response in a more limited domain (25°–80°N, 130°–30°W) for the pentad mean following each MJO phase. Comparing their results with the fast and slow composites shown previously, we find that for phases 1–4, the responses generally resemble our fast episode response, but for phases 7 and 8 their patterns more closely resemble those of our slow response (albeit with much weaker

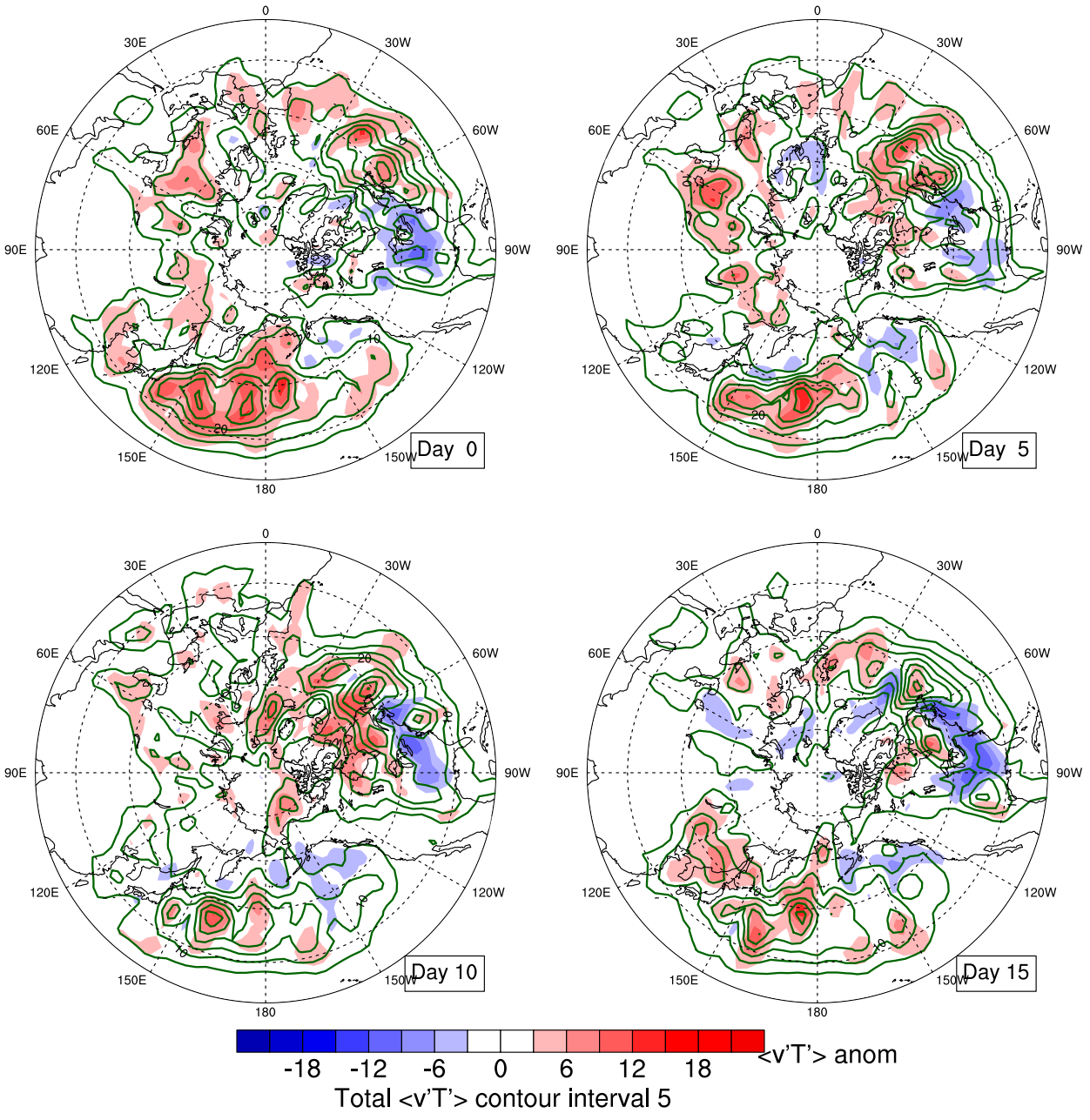

FIG. 11. Slow episode composites of covariance between high-pass meridional wind and temperature at 850 hPa (periods less than 10 days retained) for MJO phase 4 at lags 0, +5, +10, and +15 days (covariance lag MJO). Contours show total (interval of 5 m s^{-1} K), shading shows anomalies. See text for details.

amplitude). One must keep in mind that while the slow episode composites are very strong in these MJO phases, there are 3 times as many fast episodes as slow episodes, so composites based on all episodes will tend to resemble the fast responses absent a strong slow response.

b. *Relationship of fast and slow composites to weather regimes*

The remote Northern Hemisphere composite response to the fast episodes shows some clear distinctions from the composite responses to the slow episodes.

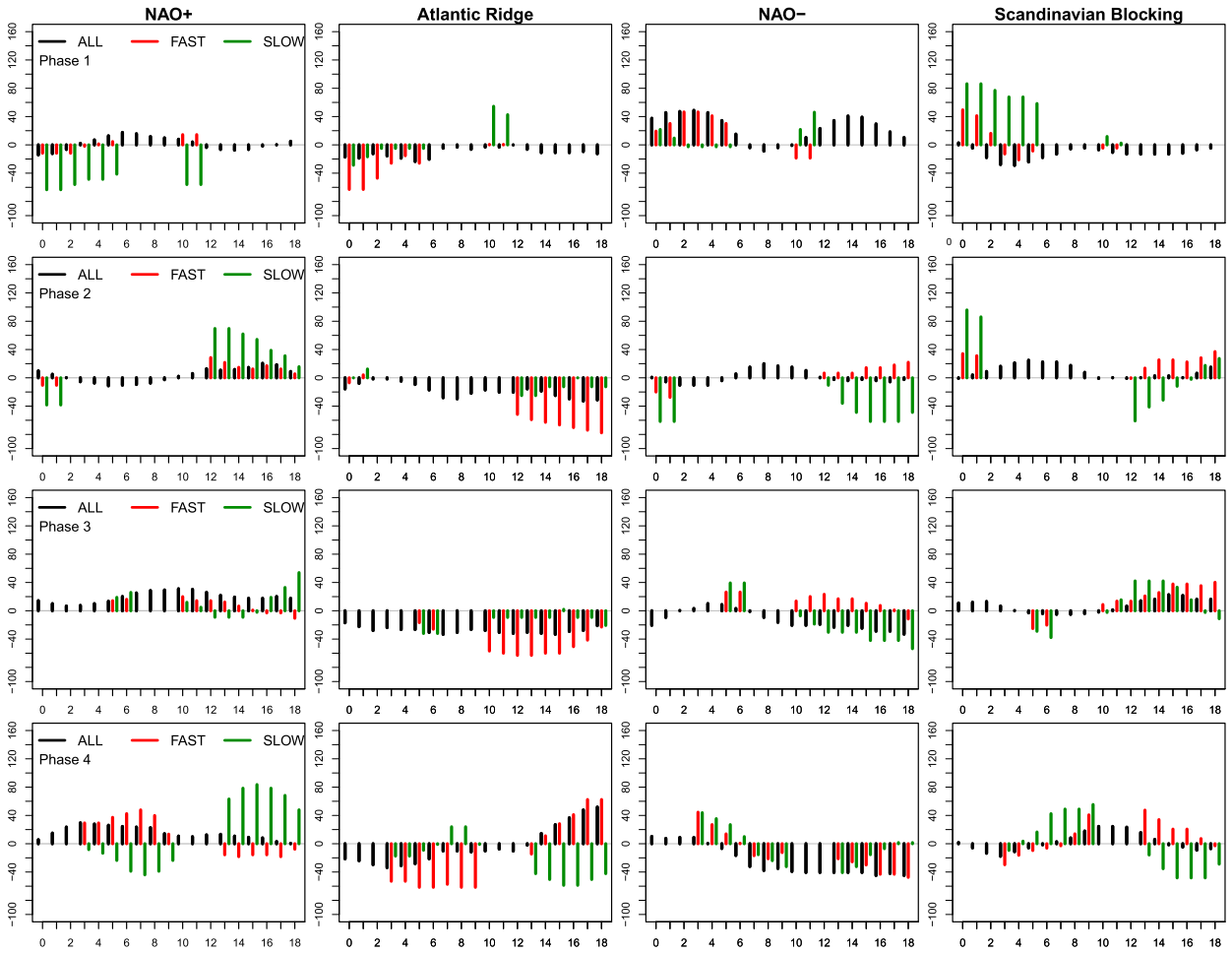

FIG. 12. Anomalous percentage occurrence of each of four Euro-Atlantic regimes as a function of lag in days for MJO phases 1–4 (with regimes lagging MJO phases). Fast episodes are shown in red bars, slow are shown in green, and all episodes are shown in black. Results that are not significant at the 90% level using a chi-squared test are not shown. See text for details of significance tests.

While the strength of the convection over the Indian Ocean is initially less for the slow episodes (Fig. 4), the residence time for convection to remain between 60° and 120°E is longer. Although the initial Z500 response to heating in both episodes is the generation of a wave train in the Pacific, its configuration is quite different in the two cases (cf. Figs. 5 and 7). While there are similarities between the fast and slow response in the Pacific–North American region in phase 4, and in the Euro-Atlantic region in phases 5 and 6, dramatic differences emerge in this region in phase 8, where the slow response is considerably larger.

Ten days after the start of phase 3, the slow episode composite response maps show an extremely clear NAO+ circulation regime response pattern, which persists until about 10 days after the start of phase 5 (not shown), when it transitions into an NAO− configuration. This is consistent with the increase in frequency of NAO+ cluster assignments (the green bars) in Figs. 12 and 13 after phases 3–5, and an even stronger increase in frequency of NAO− after phase 6. These NAO-related responses are similar to those shown by C08 and Lin et al. (2009), but are much stronger. This is because the previous studies have taken the composite responses of all MJO episodes, without regard to propagation speed. In fact if we take into account all episodes (the black bars in Fig. 12), we see a very modest increase in NAO+ with time following the onset of phase 3, similar to that reported by C08.

Our results suggest that the NAO response to the MJO is in fact due to the more slowly propagating episodes, and occurs most strongly following phases 4 and 5 of the MJO. Li and Lau (2012) discuss observational and modeling evidence indicating that the increased likelihood of the NAO− (NAO+) circulation anomaly in late winter during warm (cold) ENSO events. Understanding their results in terms of the composites we have presented for fast and slow MJO events, which have some weak conditioning on the state of ENSO, is

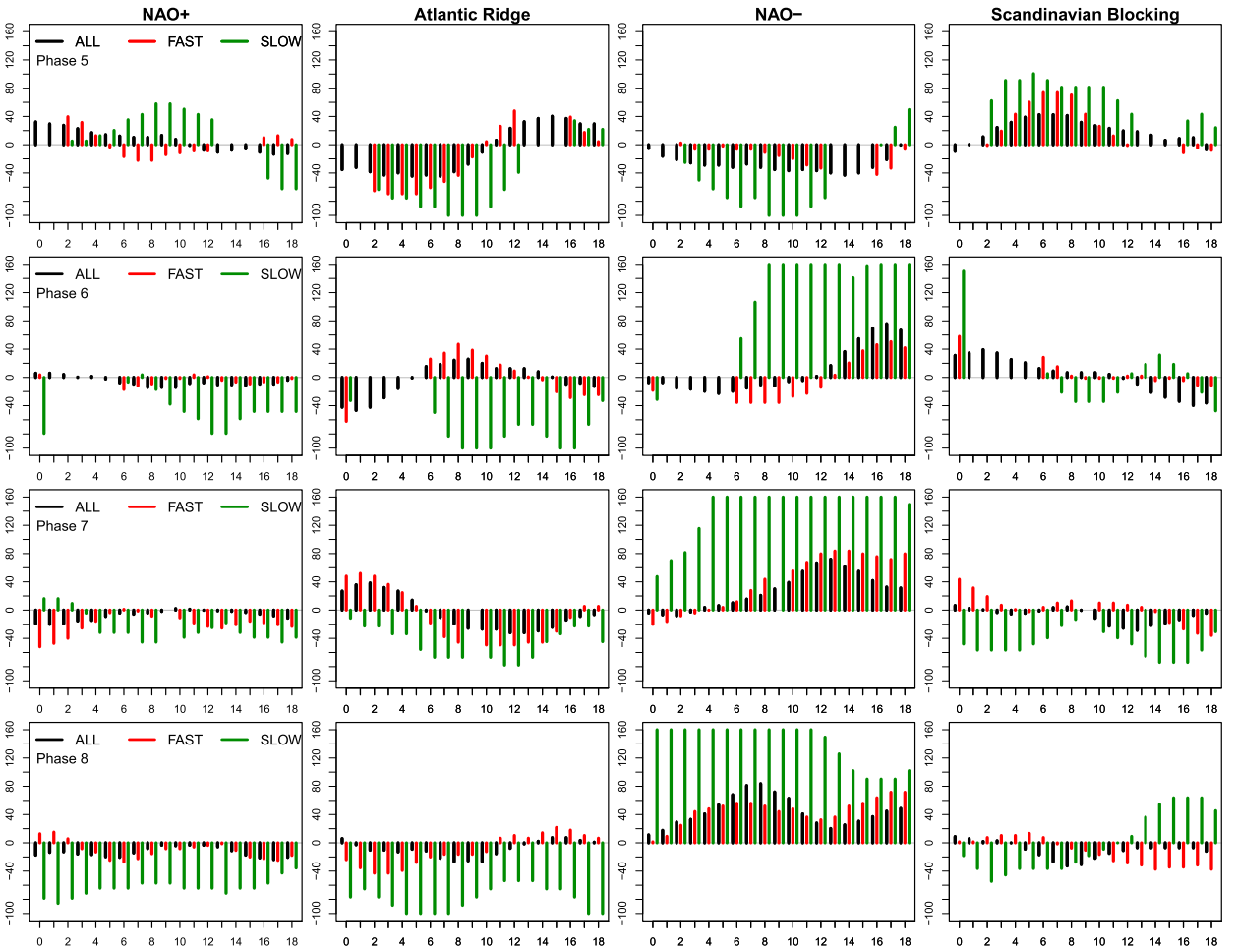

FIG. 13. Anomalous percentage occurrence of each of four Euro-Atlantic regimes as a function of lag in days for MJO phases 5–8 (with regimes lagging MJO phases). Fast episodes are shown in red bars, slow are shown in green, and all episodes are shown in black. Results that are not significant at the 90% level using a chi-squared test are not shown. See text for details of significance tests.

extremely challenging, since the events occur during both warm and cold ENSO events, and are initiated for both early and late winter, as shown in Table 1.

Riddle et al. (2013) also looked at the MJO response in terms of circulation regimes. However, that work utilizes a single set of circulation regimes in an extended area (157.5°–2.5°E) that covers much of both the PNA and EA regions. Of the seven clusters studied, at least four appear to have a strong projection on either the NAO+ or NAO− EA regimes, while still having structure in the eastern Pacific region. This makes comparison with our results difficult, since we have chosen to diagnose separate regimes entirely in the EA region.

Because of the limited observational sample size, and in particular the small number of slow episodes, our results are subject to some uncertainty. The results shown for slow and fast episodes meet the 90% significance level, as discussed in section 2. Beyond this, we have examined each slow episode individually, and find that many features of composites can be seen in each episode. In particular, 7 out of the 8 cases show a strong NAO+ response 15 days after phase 4, while 5 of the 8 cases show a strong NAO− regime response following phases 6 and 7. It was the small sample size for slow episodes that motivated us to use the standard MJO framework, which takes into account all episodes, in defining the MJO phases. The use of large ensembles of model simulations and reforecasts would allow for a much greater sample size, from which it would be appropriate (and perhaps more insightful) to recompute the MJO phases separately for slow and fast episodes.

7. Summary and conclusions

Fast and slow MJO episodes have been diagnosed from reanalysis winds and observed OLR, and the

remote responses distinguished in terms of composites of the midlevel geopotential height field, the upper-level streamfunction and phase-independent wave activity flux, and the frequency of occurrence of circulation regimes in the Euro-Atlantic regions. Slow episodes are distinguished by MJO-related heating having a longer residence time over the Maritime Continent (MJO phases 4–5), and taking over 20 days to propagate to the western Pacific (MJO phase 6). Fast episodes are distinguished by more intense heating in the Indian Ocean initially, but then a rapid propagation (less than 10 days) to phase 6. In terms of the remote response we find the following:

- The midlevel height field anomaly composite for fast episodes show rapid development of a wave train in the PNA region, followed by some downstream propagation into the Euro-Atlantic region. A signature of the NAO+ regime is seen associated with phases 4 and 5 of the MJO.
- For slow episodes, the midlevel height anomaly composite initially shows both the development of the low heights over the Gulf of Alaska followed by a strong projection onto the NAO+ regime. This strong projection of the composite anomalies is confirmed by a dramatic increase in the frequency of occurrence of the NAO+ regime 15 days following phase 4. The frequency of occurrence of NAO− following phase 6 increases sharply, in agreement with the very strong composite anomaly fields.
- The modest increase in NAO+ frequency for all strong episodes (total category) for phase 3 after about 10 days agrees with previous work, but the strong increases in frequency of occurrence of the NAO+ regime seen in the slow episodes after phases 4–5 are new.
- The slow episode changes for NAO− in phase 6 are much larger than seen previously for all episodes, indicating that this response is dominated by slow MJO episodes.
- The horizontal components of the phase-independent wave activity flux at 250 hPa show baroclinic source regions in the subtropical and midlatitude central Pacific for both slow and fast episodes. For the slow episodes, this source (following MJO phase 3) is coincident with enhanced storm-track activity, as measured by the 850-hPa meridional heat flux by high-frequency eddies. This suggests that the storm tracks play an important role in enhancing the NAO response, although more detailed analysis of this link is needed.

Acknowledgments. This work was supported by the Office of Naval Research under Award N00014-21-1-0449. DMS was also supported by NSF Grant AGS-1338427, NOAA Grant NA14OAR4310160, and NASA Grant NNX14AM19G.

REFERENCES

Branstator, G. W., 2014: Long-lived response of the midlatitude circulation and storm tracks to pulses of tropical heating. *J. Climate*, **27**, 8809–8826, doi:10.1175/JCLI-D-14-00312.1.

Cassou, C., 2008: Intraseasonal interaction between the Madden–Julian Oscillation and the North Atlantic Oscillation. *Nature*, **455**, 523–527, doi:10.1038/nature07286.

Christiansen, B., 2007: Atmospheric circulation regimes: Can cluster analysis provide the number? *J. Climate*, **20**, 2229–2250, doi:10.1175/JCLI4107.1.

Dee, D., and Coauthors, 2011: The ERA-Interim reanalysis: Configuration and performance of the data assimilation system. *Quart. J. Roy. Meteor. Soc.*, **137**, 553–597, doi:10.1002/qj.828.

Henderson, S., E. Maloney, and E. Barnes, 2016: The influence of the Madden–Julian Oscillation on Northern Hemisphere winter blocking. *J. Climate*, **29**, 4597–4616, doi:10.1175/JCLI-D-15-0502.1.

Kim, D., J.-S. Kug, and A.-H. Sobel, 2014: Propagating versus nonpropagating Madden–Julian Oscillation events. *J. Climate*, **27**, 111–125, doi:10.1175/JCLI-D-13-00084.1.

Kunio, Y., C. Zhang, and C. N. Long, 2013: Tracking pulses of the Madden–Julian Oscillation. *Bull. Amer. Meteor. Soc.*, **94**, 1871–1891, doi:10.1175/BAMS-D-12-2000157.1.

Li, Y., and N.-C. Lau, 2012: Impact of ENSO on the atmospheric variability over the North Atlantic in late winter—Role of transient eddies. *J. Climate*, **25**, 320–342, doi:10.1175/JCLI-D-11-00037.1.

Liebmann, B., and C. A. Smith, 1996: Description of a complete (interpolated) outgoing longwave radiation dataset. *Bull. Amer. Meteor. Soc.*, **77**, 1275–1277.

Lin, H., G. Brunet, and J. Derome, 2008: Forecast skill of the Madden–Julian Oscillation in two Canadian atmospheric models. *Mon. Wea. Rev.*, **136**, 4130–4149, doi:10.1175/2008MWR2459.1.

——, ——, and ——, 2009: An observed connection between the North Atlantic Oscillation and the Madden–Julian Oscillation. *J. Climate*, **22**, 364–380, doi:10.1175/2008JCLI2515.1.

——, ——, and R. Mo, 2010: Impact of the Madden–Julian Oscillation on wintertime precipitation in Canada. *Mon. Wea. Rev.*, **138**, 3822–3839, doi:10.1175/2010MWR3363.1.

Matthews, A. J., B. J. Hoskins, and M. Masutani, 2004: The global response to tropical heating in the Madden–Julian Oscillation during northern winter. *Quart. J. Roy. Meteor. Soc.*, **130**, 1991–2011, doi:10.1256/qj.02.123.

Michelangeli, P.-A., R. Vautard, and B. Legras, 1995: Weather regimes: Recurrence and quasi stationarity. *J. Atmos. Sci.*, **52**, 1237–1256, doi:10.1175/1520-0469(1995)052<1237:WRRAQS>2.0.CO;2.

Moore, R. W., O. Martius, and T. Spengler, 2010: The modulation of the subtropical and extratropical atmosphere in the Pacific basin in response to the Madden–Julian Oscillation. *Mon. Wea. Rev.*, **138**, 2761–2779, doi:10.1175/2010MWR3194.1.

Mundhenk, B. D., E. A. Barnes, and E. D. Maloney, 2016: All-season climatology and variability of atmospheric river frequencies over the North Pacific. *J. Climate*, **29**, 4885–4903, doi:10.1175/JCLI-D-15-0655.1.

Riddle, E. E., M. B. Stoner, N. C. Johnson, M. L. L'Heureux, D. C. Collins, and S. B. Feldstein, 2013: The impact of the MJO on

clusters of wintertime circulation anomalies over the North American region. *Climate Dyn.*, **40**, 1749–1766, doi:10.1007/s00382-012-1493-y.

Seo, K.-H., and S.-W. Son, 2012: The global atmospheric circulation response to tropical diabatic heating associated with the Madden–Julian Oscillation during northern winter. *J. Atmos. Sci.*, **69**, 79–96, doi:10.1175/2011JAS3686.1.

Straus, D. M., 1983: On the role of the seasonal cycle. *J. Atmos. Sci.*, **40**, 303–313, doi:10.1175/1520-0469(1983)040<0303:OTROTS>2.0.CO;2.

——, 2010: Synoptic-eddy feedbacks and circulation regime analysis. *Mon. Wea. Rev.*, **138**, 4026–4034, doi:10.1175/2010MWR3333.1.

——, S. Corti, and F. Molteni, 2007: Circulation regimes: Chaotic variability versus SST-forced predictability. *J. Climate*, **20**, 2251–2272, doi:10.1175/JCLI4070.1.

——, E. Swenson, and C.-L. Lappen, 2015: The MJO cycle forcing of the North Atlantic circulation: Intervention experiments with the Community Earth System Model. *J. Atmos. Sci.*, **72**, 660–681, doi:10.1175/JAS-D-14-0145.1.

Takaya, K., and H. Nakamura, 2001: A formulation of a phase-independent wave-activity flux for stationary and migratory quasi-geostrophic eddies in a zonally varying basic flow. *J. Atmos. Sci.*, **58**, 608–627, doi:10.1175/1520-0469(2001)058<0608:AFOAPI>2.0.CO;2.

Vautard, R., 1990: Multiple weather regimes over the North Atlantic: Analysis of precursors and successors. *Mon. Wea. Rev.*, **118**, 2056–2081, doi:10.1175/1520-0493(1990)118<2056:MWROTN>2.0.CO;2.

Ventrice, M. J., M. C. Wheeler, H. H. Hendon, C. J. Schreck, C. D. Thorncroft, and G. N. Kiladis, 2013: A modified multivariate Madden–Julian oscillation index using velocity potential. *Mon. Wea. Rev.*, **141**, 4197–4210, doi:10.1175/MWR-D-12-00327.1.

Vitart, F., and F. Molteni, 2010: Simulation of the Madden–Julian Oscillation and its teleconnections in the ECMWF forecast system. *Quart. J. Roy. Meteor. Soc.*, **136**, 842–855, doi:10.1002/qj.623.

Waliser, D., and Coauthors, 2009: MJO simulation diagnostics. *J. Climate*, **22**, 3006–3030, doi:10.1175/2008JCLI2731.1.

Wang, W., M.-P. Hung, S. J. Weaver, A. Kumar, and X. Due, 2014: MJO prediction in the NCEP Climate Forecast System version 2. *Climate Dyn.*, **42**, 2509–2520, doi:10.1007/s00382-013-1806-9.

Wheeler, M. C., and H. H. Hendon, 2004: An all-season real-time multivariate MJO index: Development of an index for monitoring and prediction. *Mon. Wea. Rev.*, **132**, 1917–1932, doi:10.1175/1520-0493(2004)132<1917:AARMMI>2.0.CO;2.

Wu, C.-H., and H.-H. Hsu, 2009: Topographic influence of the MJO in the Maritime Continent. *J. Climate*, **22**, 5433–5448, doi:10.1175/2009JCLI2825.1.

Zhang, C., 2005: Madden–Julian Oscillation. *Rev. Geophys.*, **43**, RG2003, doi:10.1029/2004RG000158.